

Banner appropriate to article type will appear here in typeset article

Two-Dimensional Vesicle Hydrodynamics from Hydrophobic Attraction Potential

Szu-Pei Fu¹, Bryan Quaife², Rolf Ryham¹, and Yuan-Nan Young³

¹Department of Mathematics,
Fordham University, Bronx, New York 10458, USA

²Department of Scientific Computing,
Florida State University, Tallahassee, Florida 32306, USA

³Department of Mathematical Sciences, New Jersey Institute of Technology,
Newark, New Jersey 07102, USA

(Received xx; revised xx; accepted xx)

We develop a new model, to our knowledge, for the many-body hydrodynamics of amphiphilic Janus particles suspended in a viscous background flow. The Janus particles interact through a hydrophobic attraction potential that leads to self-assembly into bilayer structures. We adopt an efficient integral equation method for solving the screened Laplace equation for hydrophobic attraction and for solving the mobility problem for hydrodynamic interactions. The integral equation formulation accurately captures both interactions for near touched boundaries. Under a linear shear flow, we observe the tank-treading deformation in a two-dimensional vesicle made of Janus particles. The results yield measurements of inter-monolayer friction, membrane permeability, and at large shear rates, membrane rupture. The simulations studies include a vesicle in parabolic flow and vesicle-vesicle interactions in shear and extensional flows. The hydrodynamics of the Janus particles vesicle replicate the behaviour of an inextensible elastic vesicle membrane.

Key words: Authors should not enter keywords on the manuscript, as these must be chosen by the author during the online submission process and will then be added during the typesetting process (see [Keyword PDF](#) for the full list). Other classifications will be added at the same time.

MSC Codes (*Optional*) Please enter your MSC Codes here

1. Introduction

Described by physicist Pierre-Gilles de Gennes as “another animal in soft matter physics”, the Janus particle—often a spherical particle with a hydrophobic and a hydrophilic hemisphere—exhibits complex aggregate, clustering, and self-assembly into mesoscopic and macroscopic structures that are relevant to a wide range of applications in biology and bioengineering

Abstract must not spill onto p.2

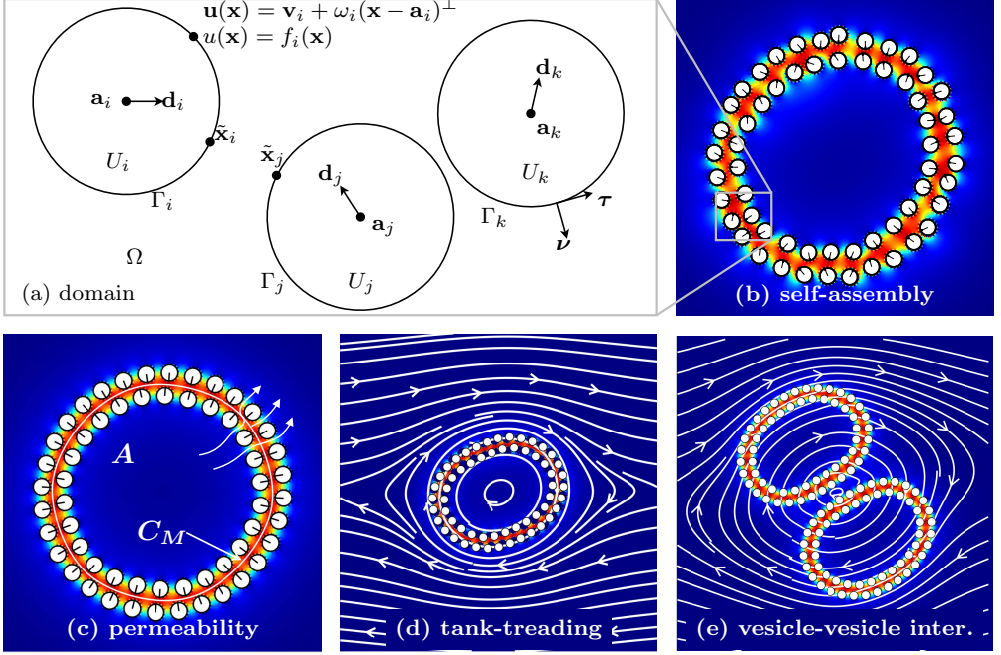


Figure 1: Panel (a) illustrates the domain and boundary conditions for the mobility problem. The color map in panels (b)–(e) is the solution u of (2.8). Red is for $u = 1$ and blue is for $u = 0$. Particles self-assemble into vesicle bilayers (panel (b)) and eventually arrange along inner and outer leaflets. In panel (c), C_M is the midplane curve, A is the enclosed area, and L is the arc length. Initially stretched vesicles relax to equilibrium with fluid flow across the bilayer. The study considers a single vesicle in background flows such as shear flow (panel (d)) and hydrodynamic vesicle-vesicle interactions (panel (e)).

(de Gennes (1991)). Whether it is surface chemistry or polarity under an external field, the dynamics of Janus particles in a viscous solvent is inevitably the combination of long-range hydrodynamics interactions with both short- and intermediate-range particle-particle interactions. Such multi-scale nature of Janus particle dynamics underlies the richness of a Janus particle suspension, as de Gennes (1991) suggested by the example of a “thin film of Janus grains” that can breathe due to the interstices between Janus particles.

Recently, Fu *et al.* (2020) illustrated that the hydrophobic interactions between Janus particles (JP) in a viscous solvent can be used as a coarse-grained model to capture the mechanics of an elastic bilayer membrane of amphiphilic macromolecules such as lipids. Depending on their total number and geometry, JP suspensions can aggregate to form a micelle, a patch of bilayer membrane with open ends, and a self-enclosed bilayer membrane, referred to as a JP vesicle. Using a hybrid continuum model for the interactions between amphiphilic particles in a viscous solvent and with a boundary integral formulation, Fu *et al.* (2020) showed that the granularity of membrane remodeling, as occurs during fusion and fission of bilayers, can be accurately captured by the coarse-grained model.

In the present work, we extend the hybrid continuum model in Fu *et al.* (2020) for the Janus suspension to incorporate the collective hydrodynamics of a Janus suspension under various flows. The JP vesicles in our simulations replicate well-known vesicle hydrodynamics such as tank-treading and inter-leaflet slippage in a shear flow and migration in Poiseuille flow from continuum models. Furthermore we use the hybrid continuum model to investigate

permeability and rupture of a bilayer membrane due to an imposed flow. Finally, we compare a pair of interacting JP vesicles with a continuum model of a pair of vesicles.

Brandner *et al.* (2019) used the coarse-grained force field with a lattice Boltzmann molecular dynamics to simulate the hydrodynamics of a nano-sized vesicle under a shear flow. In MD simulations, the hydrodynamic interactions for the solvent phase are often approximated by an implicit solvent coarse-grained model. In the present work, the hydrodynamic interactions come from the mobility problem for the Stokes equations for the incompressible, viscous solvent.

We require a numerical method to avoid unphysical contact between rigid Janus particles. Optimization-based contact methods introduce constraints, such as enforcing a non-positive space-time interference volume (Lu *et al.* (2017); Bystricky *et al.* (2020); Yan *et al.* (2020)). These methods do not introduce stiffness, but do require solving potentially expensive nonlinear complementarity problems at each time step. Repulsion-based contact methods, which we employ, introduce an artificial repulsion force that increases in strength as two particles approach one another (Glowinski *et al.* (2001); Feng & Michaelides (2004); Kabacoglu *et al.* (2018)). Strong repulsion forces can introduce numerical stiffness, but with the presence of the hydrophobic forces, we maintain contact-free suspensions with a relatively weak non-stiff repulsive force.

The paper is organized as follows. In § 2 we present the formulation for the Janus particles in a viscous fluid in the zero-Reynolds number regime (Figure 1a). In § 3 we extend the hybrid continuum model for a Janus suspension to include the effects of a far-field flow via the mobility problem formulation. In § 4 we validate our model and present simulation results for a single JP vesicle (Figure 1d) and for a pair of JP vesicles (Figure 1e) under various flowing conditions. Finally we provide discussion and outlook for future directions in § 5.

2. Governing Equations

2.1. Mobility Problem

The objective of this work is to study the hydrodynamics of JP vesicles in background flows. We consider an N_b -many body collection of JP suspended in a two-dimensional unbounded domain Ω . The boundary of each particle is denoted by Γ_i so that $\partial\Omega = \Gamma_1 \cup \Gamma_2 \cup \dots \cup \Gamma_{N_b}$ (Figure 1a). Assuming the inertial terms are negligible, the governing equations are

$$-\mu\Delta\mathbf{u} + \nabla p = \mathbf{0}, \quad \mathbf{x} \in \Omega, \quad (2.1)$$

$$\nabla \cdot \mathbf{u} = 0, \quad \mathbf{x} \in \Omega, \quad (2.2)$$

$$\mathbf{u} - \mathbf{u}_\infty \rightarrow \mathbf{0}, \quad |\mathbf{x}| \rightarrow \infty, \quad (2.3)$$

where \mathbf{u} is the velocity, p is the pressure, \mathbf{u}_∞ is the background flow, and μ is the constant viscosity. Since each particle Γ_i with centre \mathbf{a}_i is a rigid body, its velocity satisfies

$$\mathbf{v}(\mathbf{x}) = \mathbf{v}_i + \omega_i(\mathbf{x} - \mathbf{a}_i)^\perp, \quad \mathbf{x} \in \Gamma_i, \quad (2.4)$$

where \mathbf{v}_i is its translational velocity and ω_i is its angular velocity. Here, $\langle x, y \rangle^\perp = \langle -y, x \rangle$. Therefore, the no-slip boundary condition on each particle is

$$\mathbf{u}(\mathbf{x}) = \mathbf{v}_i + \omega_i(\mathbf{x} - \mathbf{a}_i)^\perp, \quad \mathbf{x} \in \Gamma_i. \quad (2.5)$$

To determine the translational and angular velocities of each particle, we define imposed forces \mathbf{F}_i and torques T_i acting on each particle. Since the small particles are inertialess,

force and torque balance gives

$$\mathbf{F}_i - \int_{\Gamma_i} \boldsymbol{\sigma} \cdot \boldsymbol{\nu} \, ds = \mathbf{0}, \quad i = 1, \dots, N_b, \quad (2.6)$$

$$T_i - \int_{\Gamma_i} (\mathbf{x} - \mathbf{a}_i)^\perp \cdot (\boldsymbol{\sigma} \cdot \boldsymbol{\nu}) \, ds = 0, \quad i = 1, \dots, N_b, \quad (2.7)$$

where $\boldsymbol{\sigma} = -p\mathbf{I} + \mu(\nabla\mathbf{u} + \nabla\mathbf{u}^T)$ is the hydrodynamic stress tensor (pressure tensor) and $\boldsymbol{\nu}_i$ is the particle outward normal. The process of finding the translational and angular velocities given the forces and torques is referred to as the mobility problem.

2.2. Imposed Forces

The imposed forces and torques contain two parts: hydrophobic attraction and repulsion. The hydrophobic attraction potential was introduced by Fu *et al.* (2020) and is responsible for forming particle aggregates that sequester their hydrophobic surface regions (Figure 1b). We model hydrophobic attraction by solving the screened Laplace equation boundary value problem

$$-\rho^2 \Delta u + u = 0, \quad \mathbf{x} \in \Omega, \quad (2.8)$$

$$u(\mathbf{x}) = f_i(\mathbf{x}), \quad \mathbf{x} \in \Gamma_i, \quad i = 1, \dots, N_b, \quad (2.9)$$

$$u \rightarrow 0, \quad |\mathbf{x}| \rightarrow \infty, \quad (2.10)$$

where $0 \leq f_i \leq 1$ is a material label with $f_i = 0$, respectively 1, representing hydrophilic, respectively hydrophobic, portions of the surface. We assume that both f_i and Γ_i are smooth. The parameter $\rho > 0$ is the decay length of attraction. The forces and torques of attraction are

$$\mathbf{F}_i^{\text{hydro}} = \int_{\Gamma_i} \mathbf{T} \cdot \boldsymbol{\nu} \, ds, \quad T_i^{\text{hydro}} = \int_{\Gamma_i} (\mathbf{x} - \mathbf{a}_i)^\perp \cdot (\mathbf{T} \cdot \boldsymbol{\nu}) \, ds, \quad (2.11)$$

where

$$\mathbf{T} = \gamma \rho^{-1} u^2 \mathbf{I} + 2\rho\gamma \left(\frac{1}{2} |\nabla u|^2 \mathbf{I} - \nabla u \nabla u^T \right) \quad (2.12)$$

is the hydrophobic stress tensor and $\gamma > 0$ is the interfacial tension.

The second part of the imposed forces and torques comes from repulsion between proximal particles. Given a pair particles indexed with i and j , we find the two points $\tilde{\mathbf{x}}_i \in \Gamma_i$ and $\tilde{\mathbf{x}}_j \in \Gamma_j$ that are closest to one another (Figure 1a). We then define the repulsion force and torque

$$\mathbf{F}_i^{\text{repul}} = \sum_{j \neq i} \frac{\tilde{\mathbf{x}}_i - \tilde{\mathbf{x}}_j}{|\tilde{\mathbf{x}}_i - \tilde{\mathbf{x}}_j|} P'(|\tilde{\mathbf{x}}_i - \tilde{\mathbf{x}}_j|), \quad (2.13)$$

$$T_i^{\text{repul}} = \sum_{j \neq i} (\tilde{\mathbf{x}}_i - \mathbf{a}_i)^\perp \cdot \frac{\tilde{\mathbf{x}}_i - \tilde{\mathbf{x}}_j}{|\tilde{\mathbf{x}}_i - \tilde{\mathbf{x}}_j|} P'(|\tilde{\mathbf{x}}_i - \tilde{\mathbf{x}}_j|). \quad (2.14)$$

The repulsion profile $P(r)$ is set to zero for distances r larger than a repulsion length scale ρ_0 . As such, (2.13) and (2.14) ignore particles outside a ρ_0 -tubular neighborhood of Γ_i . For $0 \leq r < \rho_0$, we use $P(r) = M(1 - \sin(r/\rho_0))$ where M is sufficiently large to prevent particle collisions. Then, the total imposed force and torque are

$$\mathbf{F}_i = \mathbf{F}_i^{\text{hydro}} + \mathbf{F}_i^{\text{repul}}, \quad T_i = T_i^{\text{hydro}} + T_i^{\text{repul}}, \quad i = 1, \dots, N_b. \quad (2.15)$$

2.3. Time Marching

By solving the mobility problem, we obtain translational and angular velocities of the N_b -body system. A second-order Adams-Bashforth scheme updates the particle positions and orientations. By including the repulsion force (2.13), particle collisions are avoided even when using a relatively large time step.

3. Integral Equation Method

Computing the hydrophobic attraction potential and the particle forces and torques requires the solution of elliptic partial differential equations (PDEs) in an unbounded complex domain. We recast both these PDEs as boundary integral equations (BIEs). We discretize each BIE at N points on each of the N_b particles with a collocation method. Integrals that are smooth are computed with the spectrally-accurate trapezoid rule, and nearly-singular integrals, caused by close contact between two particles, are computed with a high-order interpolation-based quadrature rule (Quaife & Biros (2014)). After discretizing and applying quadrature, the resulting linear system is solved with matrix-free GMRES, and we guarantee that the number of GMRES iterations is mesh-independent by using second-kind BIEs.

3.1. HAP Boundary Integral Equation

Similar to our previous work (Fu *et al.* (2020)), we represent the HAP as a double-layer potential

$$u(\mathbf{x}) = \frac{1}{2\pi} \int_{\partial\Omega} \frac{\partial}{\partial \nu_{\mathbf{y}}} K_0 \left(\frac{|\mathbf{x} - \mathbf{y}|}{\rho} \right) \sigma(\mathbf{y}) \, ds_{\mathbf{y}}, \quad \mathbf{x} \in \Omega, \quad (3.1)$$

where K_0 is the zeroth-order modified Bessel function of the first kind and the integral is taken in the sense of principle value whenever $\mathbf{x} \in \partial\Omega$. By requiring that the density function σ satisfies the second-kind integral equation

$$f(\mathbf{x}) = \frac{1}{2} \sigma(\mathbf{x}) + \frac{1}{2\pi} \int_{\partial\Omega} \frac{\partial}{\partial \nu_{\mathbf{y}}} K_0 \left(\frac{|\mathbf{x} - \mathbf{y}|}{\rho} \right) \sigma(\mathbf{y}) \, ds_{\mathbf{y}}, \quad \mathbf{x} \in \partial\Omega, \quad (3.2)$$

the HAP double-layer potential (3.1) satisfies the screened Laplace equation (2.8)–(2.10). After discretizing (3.2), the result is an $NN_b \times NN_b$ linear system that is solved with block-diagonal preconditioned GMRES.

To calculate the hydrophobic force and torque, the gradient of the double-layer potential (3.1) must be computed on the boundary of each particle. The resulting integrands are singular, and specialized quadrature would be necessary to approximate such integrals. Alternatively, in Section 3.3, we show how the force and torque calculations can be expressed in terms of non-singular integrals.

3.2. Mobility Problem Boundary Integral Equation

Following previous work of Bystricky *et al.* (2020), we use the velocity representation of Power & Miranda (1987). In particular, we write the velocity as the sum of a double-layer potential and N_b -many Stokeslets and rotlets

$$\mathbf{u}(\mathbf{x}) = \mathbf{u}_{\infty}(\mathbf{x}) + \mathcal{D}[\boldsymbol{\eta}](\mathbf{x}) + \sum_{i=1}^{N_b} (\mathbf{S}(\mathbf{x}, \mathbf{a}_i) \mathbf{F}_i + \mathbf{R}(\mathbf{x}, \mathbf{a}_i) T_i), \quad \mathbf{x} \in \Omega. \quad (3.3)$$

The double-layer potential is

$$\mathcal{D}[\boldsymbol{\eta}](\mathbf{x}) = \frac{1}{\pi} \int_{\partial\Omega} \frac{\mathbf{r} \cdot \boldsymbol{\nu}}{|\mathbf{r}|^2} \frac{\mathbf{r} \otimes \mathbf{r}}{|\mathbf{r}|^2} \boldsymbol{\eta}(\mathbf{y}) \, d\mathbf{y}, \quad (3.4)$$

where $\mathbf{r} = \mathbf{x} - \mathbf{y}$ and $\rho = |\mathbf{r}|$. The Stokeslet and rotlets centred at \mathbf{a}_i are

$$\mathbf{S}(\mathbf{x}, \mathbf{a}_i) \mathbf{F}_i = \frac{1}{4\pi} \left(-\log |\mathbf{r}| + \frac{\mathbf{r} \otimes \mathbf{r}}{|\mathbf{r}|^2} \right) \mathbf{F}_i, \quad (3.5)$$

$$\mathbf{R}(\mathbf{x}, \mathbf{a}_i) T_i = \frac{1}{4\pi} \frac{\mathbf{r}^\perp}{|\mathbf{r}|^2} T_i, \quad (3.6)$$

respectively, where $\mathbf{r} = \mathbf{x} - \mathbf{a}_i$. The Stokeslet is torque-free and has force \mathbf{F}_i while the rotlet is force-free and has torque T_i . Therefore, the velocity (3.3) satisfies the total force (2.6) and torque (2.7) conditions if the double-layer potential $\mathcal{D}[\boldsymbol{\eta}]$ is force- and torque-free. Matching the limit of (3.3) with the rigid body motion, and imposing that $\mathcal{D}[\boldsymbol{\eta}]$ is force- and torque-free, the density function $\boldsymbol{\eta}$, translational velocity \mathbf{v}_i , and angular velocity ω_i satisfy

$$\begin{aligned} \mathbf{v}_i + \omega_i (\mathbf{x} - \mathbf{a}_i)^\perp &= \mathbf{u}_\infty(\mathbf{x}) - \frac{1}{2} \boldsymbol{\eta}(\mathbf{x}) + \mathcal{D}[\boldsymbol{\eta}](\mathbf{x}) \\ &+ \sum_{j=1}^{N_b} (\mathbf{S}(\mathbf{x}, \mathbf{a}_j) \mathbf{F}_j + \mathbf{R}(\mathbf{x}, \mathbf{a}_j) T_j), \quad \mathbf{x} \in \Gamma_i, \, i = 1, \dots, N_b, \end{aligned} \quad (3.7)$$

$$\int_{\partial\Gamma_i} \boldsymbol{\eta} \cdot \boldsymbol{\nu}_i \, ds = 0, \quad i = 1, \dots, N_b, \quad (3.8)$$

$$\int_{\partial\Gamma_i} \boldsymbol{\eta} \times (\mathbf{x} - \mathbf{a}_i)^\perp \cdot \boldsymbol{\nu}_i \, ds = 0, \quad i = 1, \dots, N_b. \quad (3.9)$$

After discretizing and applying appropriate quadrature rules, the result is a $(2NN_b + 3N_b) \times (2NN_b + 3N_b)$ linear system that we solve with block-diagonal preconditioned GMRES. Other BIE formulations of the mobility problem use single-layer potentials (Corona *et al.* (2017); Rachh & Greengard (2016)) or a combination of single- and double-layer potentials (Corona & Veerapaneni (2018)).

We have validated our solver for (3.7)–(3.9) using a single elliptical particle suspended in a background shear flow (see § 4.2.1). Hydrophobic attraction and repulsion are zero for a single particle (see Fu *et al.* (2020) equation 2.13). The angle of the ellipse's major axis coming from the integral equation method agrees with the theoretical, Jeffery orbit time-course (Jeffery (1922)).

3.3. Main Theoretical Result: Calculating the Hydrophobic Force

Once (3.2) has been solved for σ , we need to evaluate the integrals (2.11) which are the HAP forces and torques. These integrals involve the stress (2.12) which contains a singular integral for the gradient of the double-layer potential. To avoid singular integrals, we first define

$$v_i(\mathbf{x}) = u(\mathbf{x}) - u_i(\mathbf{x}), \quad (3.10)$$

where

$$u_i(\mathbf{x}) = \frac{1}{2\pi} \int_{\Gamma_i} \frac{\partial}{\partial \boldsymbol{\nu}_y} K_0 \left(\frac{|\mathbf{x} - \mathbf{y}|}{\rho} \right) \sigma(\mathbf{y}) \, d\mathbf{y}, \quad \mathbf{x} \in \mathbb{R}^2. \quad (3.11)$$

That is, $v_i(\mathbf{x})$ is the double-layer potential (3.1) with Γ_i excluded from $\partial\Omega$. Having defined v_i , we prove

THEOREM 1.

$$\mathbf{F}_i^{\text{hydro}} = \int_{\Gamma_i} \mathbf{J}_i \, ds, \quad T_i^{\text{hydro}} = \int_{\Gamma_i} (\mathbf{x} - \mathbf{a}_i)^\perp \cdot \mathbf{J}_i \, ds, \quad (3.12)$$

where

$$\mathbf{J}_i = 2\gamma\rho^{-1}\sigma v_i \boldsymbol{\nu} + 2\gamma\rho \frac{d\sigma}{ds} \frac{dv_i}{ds} \boldsymbol{\nu} - 2\gamma\rho \frac{d\sigma}{ds} \frac{dv_i}{d\boldsymbol{\nu}} \boldsymbol{\tau}. \quad (3.13)$$

The symbols $\boldsymbol{\tau}$ and $\frac{d}{ds}$ are the unit tangent and arc length derivative for Γ_i , respectively (Figure 1a.) The result is valid for any smooth particle shape or boundary condition. The advantage of using (3.12) over using (2.11) is that the components σ , v_i , $\frac{d\sigma}{ds}$, and $\frac{dv_i}{ds}$ of \mathbf{J}_i are smooth functions, whereas the components of (2.12) are singular integrals.

To prove (3.12), let

$$\begin{aligned} \mathbf{T} &= \mathbf{S}(u_i, u_i) + (\mathbf{S}(u_i, v_i) + \mathbf{S}(v_i, u_i)) + \mathbf{S}(v_i, v_i) \\ &= \mathbf{T}_1 + \mathbf{T}_2 + \mathbf{T}_3 \end{aligned}$$

where we introduce the bilinear form

$$\mathbf{S}(u, v) = \gamma\rho^{-1}uv\mathbf{I} + \gamma\rho\nabla u \cdot \nabla v\mathbf{I} - 2\gamma\rho\nabla u\nabla v^T. \quad (3.14)$$

Using the fact that u , u_i , and v_i solve the screened Laplace equation (2.8), and that \mathbf{T} , \mathbf{T}_j , $j = 1, 2, 3$ are symmetric, it is straightforward to verify that

$$\nabla \cdot \mathbf{T}_j = 0, \quad \nabla \cdot ((\mathbf{x} - \mathbf{a}_i)^\perp \cdot \mathbf{T}_j) = 0, \quad j = 1, 2, 3. \quad (3.15)$$

Let U_i be the interior of the particle indexed by i . For $\mathbf{x}_0 \in \Gamma_i$ and an arbitrary function $g(\mathbf{x})$, the notation

$$[[g]](\mathbf{x}_0) = \lim_{\substack{\mathbf{x} \rightarrow \mathbf{x}_0 \\ \mathbf{x} \in U_i^c}} g(\mathbf{x}) - \lim_{\substack{\mathbf{x} \rightarrow \mathbf{x}_0 \\ \mathbf{x} \in U_i}} g(\mathbf{x}), \quad (3.16)$$

denotes the jump of the limits of $g(\mathbf{x})$ taken from the outside to the inside of Γ_i .

LEMMA 1.

$$\mathbf{F}_i^{\text{hydro}} = \int_{\Gamma_i} [[\mathbf{T}_2 \boldsymbol{\nu}]] \, ds, \quad T_i^{\text{hydro}} = \int_{\Gamma_i} (\mathbf{x} - \mathbf{a}_i)^\perp \cdot [[\mathbf{T}_2 \boldsymbol{\nu}]] \, ds. \quad (3.17)$$

Proof. To show (3.17), we expand (2.11) as

$$\mathbf{F}_i = \int_{\Gamma_i} \mathbf{T}_1 \boldsymbol{\nu} + \mathbf{T}_2 \boldsymbol{\nu} + \mathbf{T}_3 \boldsymbol{\nu} \, ds. \quad (3.18)$$

By (3.10) and (3.15), we have that u_i is smooth and $\nabla \cdot \mathbf{T}_1 = \mathbf{0}$ in $\mathbb{R}^n \setminus U_i$. Similarly, $v_i = u - u_i$ is smooth and $\nabla \cdot \mathbf{T}_3 = \mathbf{0}$ in U_i . By the divergence theorem,

$$\int_{\Gamma_i} \mathbf{T}_1 \boldsymbol{\nu} \, ds = - \int_{\mathbb{R}^n \setminus U_i} \nabla \cdot \mathbf{T}_1 \, d\mathbf{x} = \mathbf{0}, \quad \int_{\Gamma_i} \mathbf{T}_3 \boldsymbol{\nu} \, ds = \int_{U_i} \nabla \cdot \mathbf{T}_3 \, d\mathbf{x} = \mathbf{0}. \quad (3.19)$$

Finally, u_i and v_i are smooth and $\nabla \cdot \mathbf{T}_2 = 0$ in U_i . This gives

$$\mathbf{0} = \int_{U_i} \nabla \cdot \mathbf{T}_2 \, d\mathbf{x} = - \int_{\Gamma_i} (\mathbf{T}_2 \boldsymbol{\nu})^- \, ds, \quad (3.20)$$

where the superscript denotes the limit taken from in U_i . Combining the above gives the first equation in (3.17). The argument for the second equation in (3.17) is identical. \square

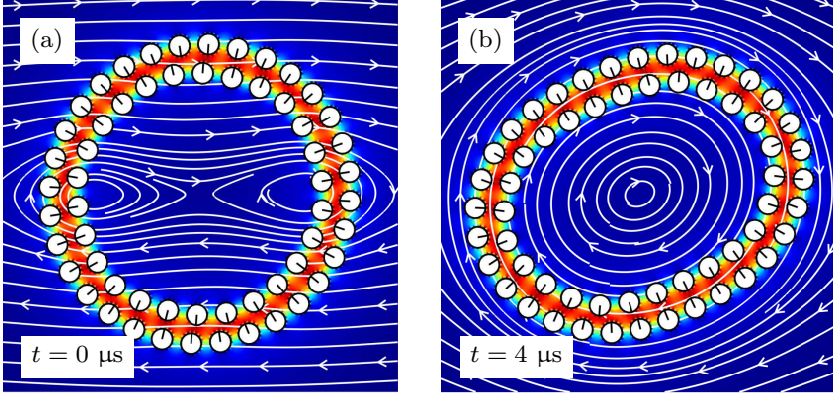


Figure 2: JP vesicles undergo tank-treading in shear flow. In panel (a), the initial, 58-body vesicle is circular and the black arrows point in the direction of the hydrophobic side of the JP. In panel (b), the JP suspension rotates and deforms with the shear flow. The color map is for the solution u of (2.8). The white curves are the streamlines of \mathbf{u} . The shear rate is $\chi = 0.0025$.

We have the following jump relations for (3.10):

$$[[u_i]] = \sigma, \quad [[v_i]] = 0, \quad [[\nabla u_i]] = \frac{d\sigma}{ds} \boldsymbol{\tau}, \quad [[\nabla v_i]] = \mathbf{0}, \quad (3.21)$$

on Γ_i (see, e.g. Klöckner *et al.* (2013)). Therefore,

$$\begin{aligned} [[\mathbf{T}_2 \mathbf{v}]] &= [[\mathbf{S}(u_i, v_i) \mathbf{v} + \mathbf{S}(v_i, u_i) \mathbf{v}]] \\ &= [[(2\gamma\rho^{-1}u_i v_i \mathbf{I} + 2\gamma\rho \nabla u_i \cdot \nabla v_i \mathbf{I} - 2\gamma\rho \nabla u_i \nabla v_i^T - 2\gamma\rho \nabla v_i \nabla u_i^T) \mathbf{v}]] \\ &= 2\gamma\rho^{-1} \sigma v_i \mathbf{v} + 2\gamma\rho \frac{d\sigma}{ds} \frac{dv_i}{ds} \mathbf{v} - 2\gamma\rho \frac{d\sigma}{ds} \frac{dv_i}{dv} \boldsymbol{\tau} = \mathbf{J}_i. \end{aligned}$$

Combining this with (3.17) gives (3.12) as required.

4. Numerical Results

4.1. Model Parameters

Fu *et al.* (2020) studied physical quantities for static JP vesicles for various particle shapes. In the present study, we fix the particle shape and vary the background flows. Specifically, the particles are circular disks with diameter $l_0 = 2.5$ nm. The boundary conditions (2.9) are $f_i(\mathbf{x}) = \frac{1}{2}(1 + \cos \theta_i)$ where θ_i is the angle between $\mathbf{x} - \mathbf{a}_i$ and \mathbf{d}_i , where the vectors \mathbf{a}_i and \mathbf{d}_i are the particle centre and director respectively. The particle diameter is the thickness of monolayers and the director points in the direction of the hydrophobic side of the JP.

We use $\rho = 2l_0$ for decay length, $\rho_0 = 0.2l_0$ for repulsion length, $M = 4.0 k_B T$ for repulsion strength, $\gamma = 4.1$ pN nm⁻¹ for interfacial tension, and $\mu = 1$ cP = 1 pN ns nm⁻² for viscosity of room-temperature water. We nondimensionalize the problem through the change of variables $t \mapsto t$ ns, $\mathbf{x} \mapsto \mathbf{x}$ nm, $\mathbf{u} \mapsto \mathbf{u}$ nm ns⁻¹, and $p \mapsto p$ pN nm⁻². The numerical time step size is $\Delta t = 0.2$.

To reach consistent simulation outcomes, we first solve for a baseline JP vesicles that is suitably close to equilibrium. We start with an assumed configuration of $N = 58$ JP in the form of two, circular, apposing monolayers of about 8 nm in radius. The norms of the translational and rotational velocities vanish exponentially with an approximate decay rate

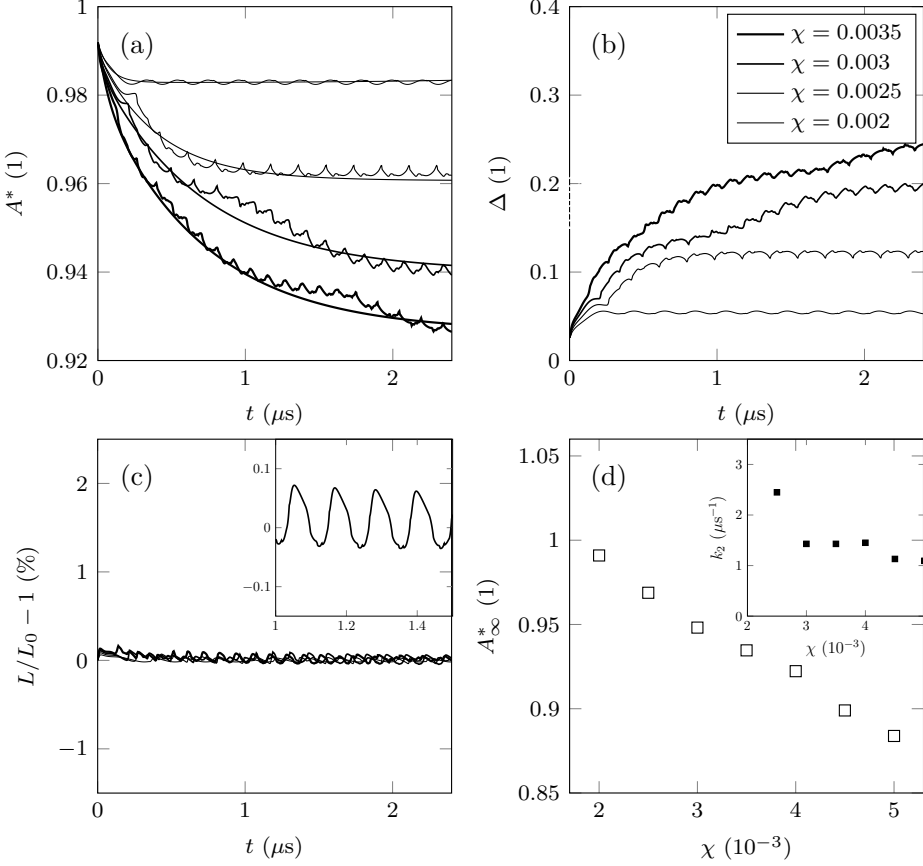


Figure 3: JP vesicles lose enclosed area but conserve length in a shear flow. Panel (a) gives the reduced area over time for four different shear rates. The monotonic curves are a two-exponential best fit. There is a commensurate increase in excess length (panel (b)), but the arc length of the mid plane curve is more or less constant for all shear rates (panel (c)). The inset in panel (c) is for shear rate 0.003. The legend in panel (b) applies to panels (a)–(c). Panel (d) plots the steady-state reduced area and the decay rate k_2 (inset) coming from the fitting data in panel (a).

$\sim 4.6 \mu\text{s}^{-1}$. An equilibrium configuration is therefore rapidly attained. This equilibrium configuration serves as the initial data in the subsequent background flow simulations.

4.2. Tank-Treading Vesicles

4.2.1. Vesicle in a Shear Flow

Our simulation studies begin by showing, for the first time, that a JP suspension with hydrophobic attraction behaves as a tank-treading vesicle (Finken *et al.* (2008); Zhao & Shaqfeh (2011)). The centroid of the baseline, 58-body JP vesicle lies at the origin and the background shear flow

$$\mathbf{u}_\infty(\mathbf{x}) = \dot{\gamma}(\mathbf{x} \cdot \mathbf{e}_y)\mathbf{e}_x, \quad (4.1)$$

is applied for shear rate $\dot{\gamma}$, and orthogonal unit vectors \mathbf{e}_x and \mathbf{e}_y for the horizontal and vertical directions, respectively. We use the dimensionless shear rate $\chi = \dot{\gamma} (\text{s}^{-1}) \text{ ns}$.

Figure 2 shows snapshots of the JP vesicle in the shear flow with $\chi = 0.0025$. Under the

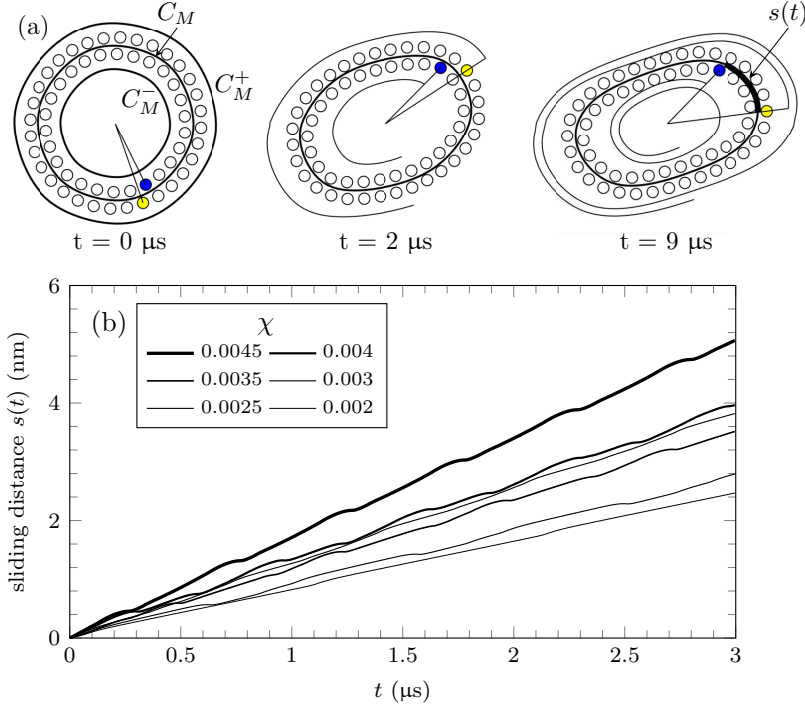


Figure 4: Inter-monolayer slip is present in the JP vesicle tank-treading motion at all shear rates. Panel (a) tracks a pair of particles (blue and yellow). The shear rate is $\chi = 0.005$ and in the right figure, the yellow particle will complete two and a quarter revolutions in the same time the blue particle completes two revolutions. The curves in panel (b) are the distance the outer leaflet has slid past the inner leaflet. The slopes of the curves give the slip velocity. With the exception of $\chi = 0.0035$, the slip velocity is generally monotonic in the shear rate.

background flow, the rigid-body boundary condition (2.5) causes the particle suspension to elongate. This perturbation disrupts the preferred particle orientations and exposes the hydrophobic core to bulk water (Figure 2, red region). In response, hydrophobic attraction (2.11) causes the particles to reorient and form a somewhat elliptically-shaped suspension. Panel (a) shows the initial configuration and panel (b) shows the later, fully-formed, clockwise tank-treading motion. The JP suspension maintains its bilayer structure throughout the simulation.

To extract physical quantities, let $A^* = 4\pi A/L^2$ be the reduced area and $\Delta = L/\sqrt{A/\pi} - 2\pi$ the excess length of the bilayer structure (Finken *et al.* (2008)). Here, A is the enclosed area and L is the total length of the JP vesicle (Figure 1a). Figure 3 shows the evolution of the area and length for various shear rates. Panels (a) and (b) show that A^* decreases and Δ increases with time, respectively, and that the rate of decrease/increase grows with shear rate. The total arc length, however, remains constant for all time for all four shear rates (panel (c)). We conclude that the JP vesicle loses area and that the bilayer behaves as a permeable membrane.

Since the starting configuration is nearly circular, the reduced area decreases from an initial value close to 1 and tends to a steady-state value A_∞^* . The data in panel (a) are fit to the model $A^* = (A_\infty^* - a_1 - a_2) + a_1 \exp(-k_1 t) + a_2 \exp(-k_2 t)$, $0 < k_2 < k_1$. Panel (d) shows that A_∞^* decreases with the shear rate. The JP vesicle achieves a steady-state reduced area

Table 1: Friction Coefficients

$\dot{\gamma}$ (ns ⁻¹)	0.0020	0.0025	0.0030	0.0035	0.0040	0.0045	0.0050
b (pN ns nm ⁻³)	0.43	1.19	0.42	0.69	0.97	0.80	1.07

earlier when the shear rate is low (inset), but the decay rate k_2 is more or less constant for higher shear rates.

The oscillations in the data of Figure 3 are due to the granularity of the JP vesicle. The inset of Figure 3c zooms in on the arc length data for the shear rate $\chi = 0.003$. It shows that the oscillations are smooth and well-resolved by our second-order Adams-Bashforth scheme.

We point out that the range of values for χ where we measured for tank-treading correspond to shear rates $\dot{\gamma} = O(10^6 \text{ s}^{-1})$ which gives fluid velocities $O(\text{m s}^{-1})$ in the vicinity of the vesicle. While large, these orders of magnitude are identical to ones used in prior MD studies (Brandner *et al.* (2019)) and are a consequence of the fact that larger shear rates are required to produce the viscous stresses needed to appreciably deform smaller vesicles.

4.2.2. Inter-Monolayer Friction

We observe inter-monolayer slip in the tank-treading, JP vesicle at all shear rates. Since they are not bound, the two leaflets of the vesicle are able to slide past one another. Monolayer slip effects have been incorporated in continuum models (Schwalbe *et al.* (2010)). In the present setting, slip is limited by viscous friction of the aqueous gaps between particles and by the constant unbinding and binding of particles pairs in apposing leaflets.

Figure 4a illustrates inter-monolayer slip by tracking the distances traveled by a pair of particles along the midplane curve. In the left image, the blue and yellow particle lie next to each other. In the right-most panel, the yellow particle has traveled farther than the blue particle. This suggests that the outer tangential velocity, obtained by projecting the velocity of the outer leaflet onto the midplane curve, is larger than that of the inner leaflet.

From the data, we obtain an inter-monolayer friction coefficient

$$b = \frac{\langle F \rangle}{\langle LU \rangle}, \quad (4.2)$$

where F is the tangential force jump, L is the length of the midplane C_M (Figure 4a), and U is the slip velocity. The time average $\langle \cdot \rangle$ is necessary to avoid division by zero whenever slip velocity vanishes.

The tangential force jump F equals the tangential shear force on the outer leaflet minus the tangential shear force on the inner leaflet. To calculate F , we first let

$$F_h = \int_{C_M^+} \boldsymbol{\tau} \cdot \boldsymbol{\sigma} \cdot \boldsymbol{\nu} \, ds - \int_{C_M^-} \boldsymbol{\tau} \cdot \boldsymbol{\sigma} \cdot \boldsymbol{\nu} \, ds \quad (4.3)$$

where C_M^+ and C_M^- are target curves obtained by projecting the midplane curve C_M a distance h outward, respectively inward, along its unit normal vector field (Figure 4a). We sample F_h for $h = \pm 1.3, \pm 1.5, \pm 1.7, \pm 1.9$ times the particle radius and define F by extrapolating to zero distance. This avoids integrating along a curve passing directly through the particles.

To calculate U , we let $u_+(\mathbf{x})$ and $u_-(\mathbf{x})$ be the tangential velocity of the outer, respectively

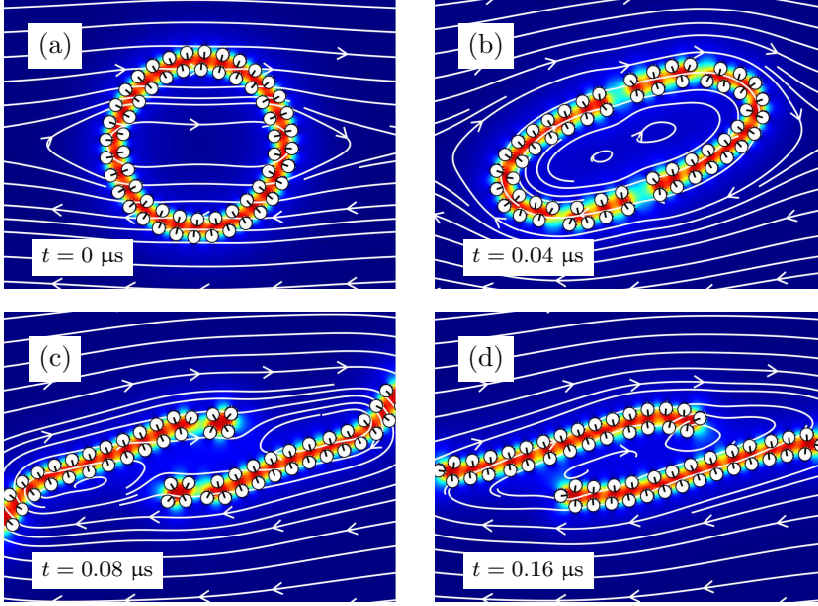


Figure 5: Tank-treading leads to membrane rupture for large shear rates.

inner, leaflet. Then

$$U = \frac{1}{L} \int_{C_M} u_+(\mathbf{x})(1 - \delta\kappa) - v_-(\mathbf{x})(1 + \delta\kappa) ds, \quad (4.4)$$

where δ is the distance from the leaflet centres to the midplane and κ is the curvature. The factors $\pm\delta\kappa$ are needed to project the leaflet velocities, defined on the particle centres, onto the midplane curve. Finally, the function $s(t) = \int_0^t dU$ records the distance one leaflet has slid past the other. Figure 4b plots the sliding distance for various shear rates.

Table 1 provides $b = 0.79 \pm 0.3$ pN ns nm⁻³ over a range of shear rates which is in good quantitative agreement with values previously reported in the literature. Atomistic studies have also considered inter-monolayer slip in lipid bilayers. Wohler & Edholm (2006) and den Otter & Shkulipa (2007) reported $b = 0.7 \times 10^6$ Pa m⁻¹ s = 0.7 pN ns nm⁻³ and $b = 2.4$ pN ns nm⁻³ for DPPC membranes simulated by MD, respectively. Using a more recent version of the Martini force field, Zgorski *et al.* (2019) gives $b = 5.5$ pN ns nm⁻³ for shear rates 0.4 ns⁻¹ and higher. It is understandable that there is uncertainty in the friction coefficients of Table 1. The scatter in our data, however, is fully consistent with that calculated from MD simulations, c.f. the transient rise in values of Table 1 and in Zgorski *et al.* (2019), Figure 10 for low shear rates.

4.2.3. Membrane Ruptures

A temporary fissure or a complete membrane rupture can occur at large shear rates. Figure 5 demonstrates how a vesicle can rupture when suspended in a shear flow. For $\chi = 0.1$, starting with a circular shape (Figure 5a), the vesicle is stretched by the background flow and fissures appear in the bilayer structure in multiple locations (Figure 5b). In Figure 5c, the ruptured vesicles form two planar micelles which are eventually carried off by the flow (Figure 5d).

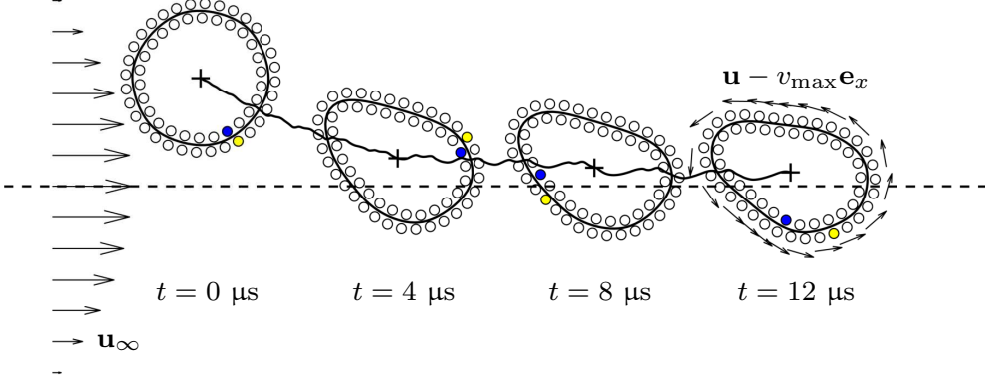


Figure 6: A JP vesicle placed in a parabolic flow drifts toward the central axis. It assumes a slipper shape and undergoes tank-treading motion like in the shear flow case. The arrows on the left illustrate the background flow and the arrows on the right show the velocity relative to the vesicle's moving frame. The thick black curve plots the distance from the axis as a function of time from left to right. The parameters are $v_{max} = 8 \text{ nm ns}^{-1}$, $w = 10$, and $R_0 = 20 \text{ nm}$.

4.2.4. Vesicle in a Parabolic Flow

Finally, we consider the parabolic background flow

$$\mathbf{u}_\infty = v_{max} \left[1 - \left(\frac{\mathbf{x} \cdot \mathbf{e}_y}{wR_0} \right)^2 \right] \mathbf{e}_x, \quad (4.5)$$

where v_{max} is the flow strength and w determines the shape of the flow. The parameter R_0 is the radius of the JP vesicle at $t = 0$ and w sets the width of the profile. Kaoui *et al.* (2009); Couplier *et al.* (2008); Danker *et al.* (2009) have shown that the behaviour of a vesicle in this unbounded flow includes vertical migration, and depending on the flow rate and reduced area, the steady-state shape can be either a symmetric parachute or an asymmetric slipper.

Figure 6 shows four configurations for one specific case where the centroid of the JP vesicle is initially placed slightly above the x -axis. We have marked a pair of particles blue and yellow in the inner and outer leaflets, respectively, and observe that the deformed JP vesicle (Figure 6, $t = 12 \mu\text{s}$) has a counterclockwise movement and the shape of the vesicle approaches an asymmetric slipper shape. For this test, the reduced area in the final configuration is approximately 0.9 which matches the previous numerical tests in Kaoui *et al.* (2009) where a slipper-like shape occurs when the flow velocity is weak and the reduced area is large. The flow causes the vesicle, which is initially placed above the axis, to drift downward where it reaches a steady height of about 1 nm.

4.3. Stretching and Permeability

Finally, we show that the JP vesicle behaves as a permeable membrane and the inextensibility comes about due to a large stretching modulus. Figures 7b shows an initial, non-equilibrium JP vesicle suspended in a quiescent flow $\mathbf{u}_\infty = 0$. The color map plots the pressure p . The red color in Figures 7b shows a spatially constant, positive internal pressure (0.05 pN nm^{-2}) and the white shows a spatially constant zero, external pressure. There is some fluid flow and the pressure vanishes as the configuration tends toward the equilibrium state (Figures 7c).

What could be the source of this drop in pressure? In membrane continuum mechanics, small changes in surface area give rise to a membrane tension $\tilde{\gamma} = K_A(A/A_0 - 1)$ where

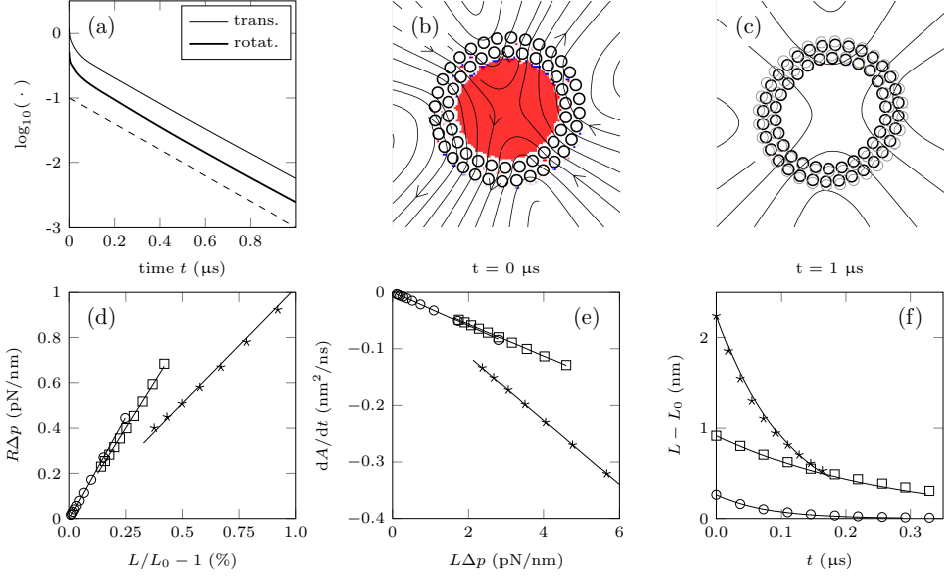


Figure 7: In JP vesicles, tension and pressure relax as fluid is expelled through the particle interstices. In panel (a), the thin curve plots the mean of the norm of the particle translational velocities. The thick curve plots the mean of the absolute value of the particle angular velocities. At $t = 0 \mu\text{s}$, the vesicle has a spatially constant internal pressure 0.05 pN nm^{-2} (red color, panel (b)). In panel (c), pressure has dissipated and the vesicle has moved from its initial configuration (gray circles), to the equilibrium configuration (black circles). The data in panels (d) and (e) support the linear relationship expressed by (4.7) and (4.8). Circles are for a vesicle with 17 nm initial radius; square are for a 34 nm initial radius. Asterisks are for a 18 nm initial radius but with smaller, 1.25 nm diameter particles. In panel (f), the theoretical time course (4.9) overlaps the data using constants K_A and P derived from panels (d) and (e).

A is the membrane surface area and A_0 is the reference surface area. The area modulus K_A of bilayers is about 240 pN nm^{-1} (Nagle & Tristram-Nagle (2000)). In the two-dimensional vesicles, the tension becomes

$$\tilde{\gamma} = K_A \left(\frac{L}{L_0} - 1 \right), \quad (4.6)$$

where L and L_0 are the vesicle arc length and resting length, respectively. Moreover, stretched, circular vesicles has a Laplace pressure

$$\Delta p = \frac{\tilde{\gamma}}{R}, \quad (4.7)$$

where Δp is the difference in internal pressure to the pressure at infinity and R^{-1} is the total curvature of the circular cylinder.

Figure 7c plots the data for the pressure jump Δp between the particle centre and the far-field (see Figures 7c and 7d). We use $R = L/(2\pi)$ for the vesicle radius, and the horizontal axis is the relative stretch. The circles are data for a vesicle with radius 17 nm. The linear fit (solid lines) shows that $R\Delta p$ is proportional to the relative stretching $L/L_0 - 1$. The squares are for a vesicle with twice the radius 34 nm, and the data overlap supports that the proportionality constant K_A is a stretching modulus that is independent of vesicle size. The data give $K_A = 170 \pm 9 \text{ pN nm}^{-1}$ which is in good agreement with the experimentally obtained

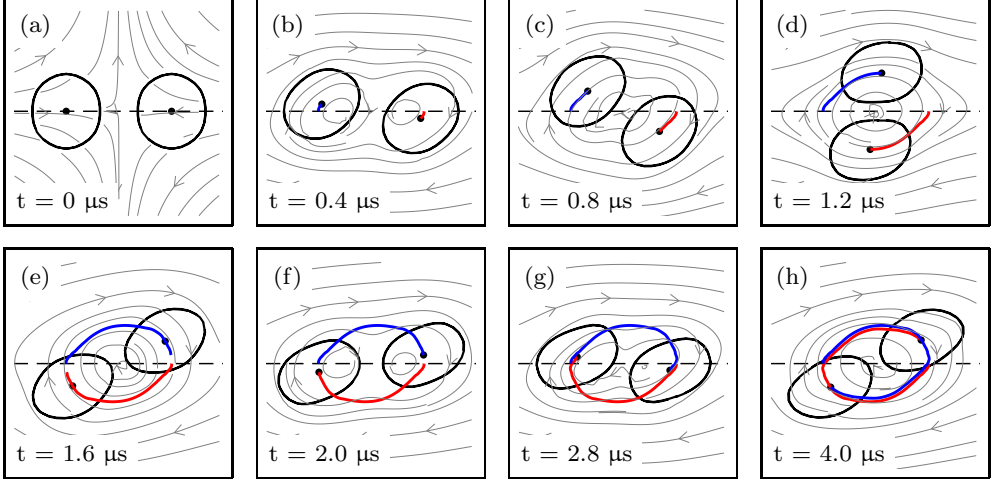


Figure 8: Two JP vesicles suspended in a shear flow interact by orbiting about the origin. The moving paths of the two centroids are plotted in blue and red. The centroids are initially located on the x -axis. The fluid velocity streamlines appear in grey. The dimensionless shear rate is $\chi = 0.005$.

area moduli of lipid bilayer. The reason the tank-treading vesicle appears inextensible (L is more or less constant in Figure 3c) is because the modulus K_A is large. To evaluate how changes to particle size lead to different physical properties, the asterisk symbols are for an 18 nm radius vesicle consisting of particles with diameter 1.25 nm, instead of the usual 2.5 nm. These data give a smaller stretching modulus of $K_A = 102 \text{ pN nm}^{-1}$.

The particles in our setup do not abut but rather have small gaps due to repulsive forces. The gaps allow for some fluid flux across the JP bilayer, and in membrane mechanics aqueous flux is quantified by the equation

$$\frac{dA}{dt} = -PL\Delta p, \quad (4.8)$$

where P is a hydraulic permeability constant (Chabanon *et al.* (2017); Quaife *et al.* (2021)). Figure 7e shows that the data for $L\Delta p$ and dA/dt obey the linear relationship expressed by (4.8). The slopes of the linear fits give the hydraulic permeabilities $P = 0.0296 \text{ nm}^3 \text{ ns}^{-1} \text{ pN}^{-1}$ and $P = 0.0283 \text{ nm}^3 \text{ ns}^{-1} \text{ pN}^{-1}$ for the 17 nm and 34 nm radius cases, respectively. Like the area modulus, the data give a permeability that is independent of vesicle size.

The hydraulic permeability we calculate, however, is not in agreement with experimentally derived values and is larger by a few orders of magnitude. We suspect this discrepancy is due to inter-particle distance of the JP being large compared to the inter-lipid spacing in real bilayers. To test this, we calculate the permeability for the particles with diameter 1.25 nm. Due to their smaller size but fixed repulsion strength, these particles have a larger inter-particle spacing resulting in an increase in permeability, $P = 0.0566 \text{ nm}^3 \text{ ns}^{-1} \text{ pN}^{-1}$ (Figure 7e, asterisk symbols).

Since the vesicles in Figure 7a are nearly circular, we can combine (4.6), (4.7), and (4.8), to derive

$$L_0(L - L(0)) + L_0^2 \ln \left| \frac{L - L_0}{L(0) - L_0} \right| = -4\pi^2 PK_A t. \quad (4.9)$$

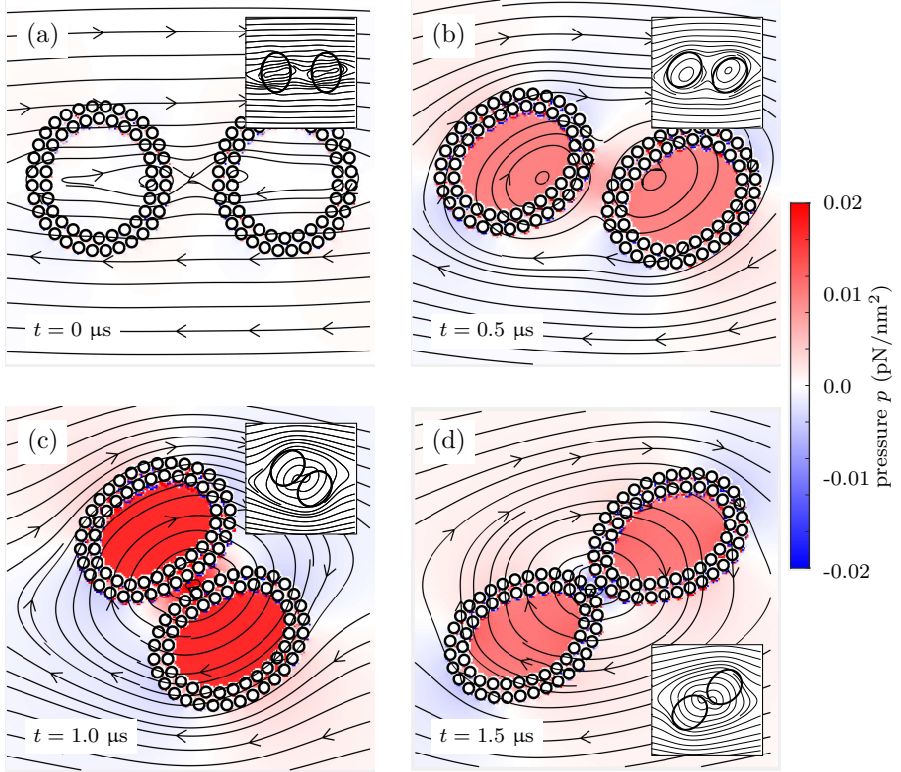


Figure 9: The figure is for the same simulation as in Figure 8, but also plots the fluid pressure p . The color bar is identical for all panels. Internal pressure is initially zero, but then grows as the vesicles come close to contact (panel (c)). The insets are generated from simulations of a continuum model of the vesicles (Quaife *et al.* (2019)). The streamlines of the two models are in agreement.

All in all, the theoretical time courses for (4.9) are in good quantitative agreement with the JP data (Figure 7f).

4.4. Two Vesicles in a Linear Flow

4.4.1. Shear Flow

Finally, we can study vesicle-vesicle interactions in background flows. Figure 8 shows the simulation of two JP vesicles suspended in a shear flow with shear rate $\chi = 0.005$. We duplicate the pre-relaxed 58-body JP vesicle from previous sections and construct the initial configuration shown in Figure 8a. The two centroids are at coordinates $(-25, 0)$ and $(25, 0)$ in nm. In all panels, the blue and red curves show the trajectory of the two JP vesicle centroids. They have nearly completed a full period by $t = 4 \mu\text{s}$.

We show snapshots of the fluid pressure in Figure 9. Since the initial JP vesicles are pre-relaxed, there is initially no pressure jump between the internal and external fluids (panel (a)). Panels (b)–(d) show the configurations when $t = \{0.5, 1, 1.5\} \mu\text{s}$, and the streamlines are plotted in the background for all panels. We include the numerical results from a continuum model in all insets and these comparisons give a qualitative agreement between two models. We also observe an adhesive effect between the two JP vesicles that is set up by the hydrophobic attraction (Figure 9c). Similar dynamics have been observed between a pair

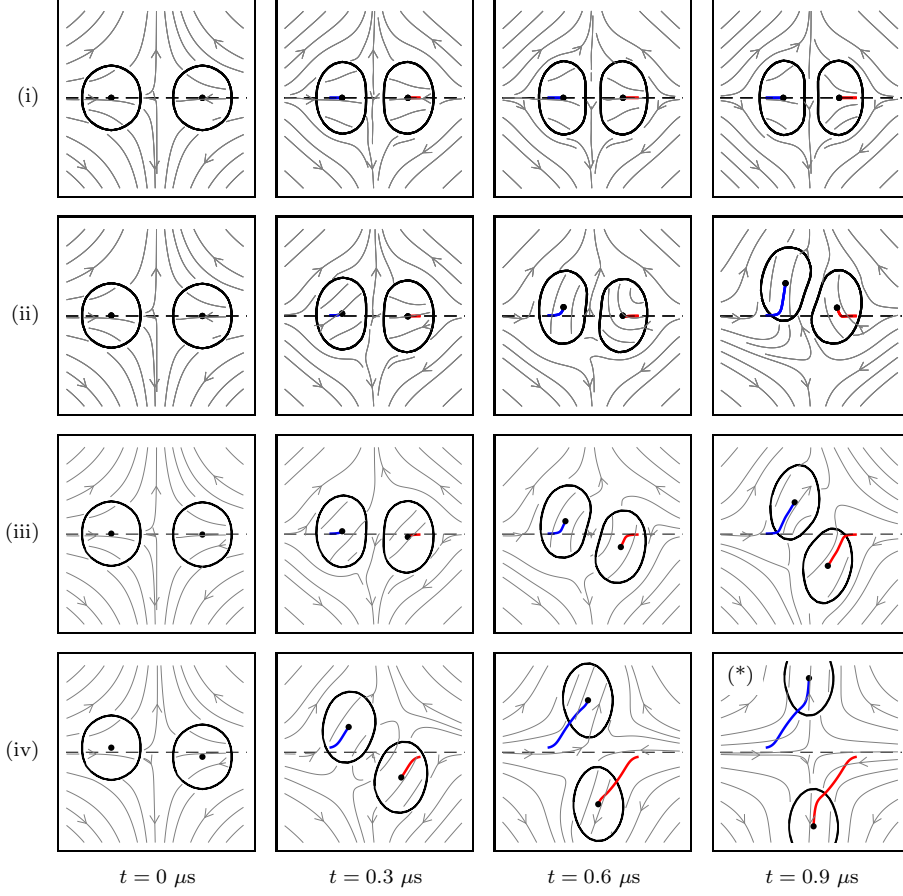


Figure 10: The initial placement of two JP vesicles suspended in an extensional flow affects the long-time dynamics. The moving paths of the two centroids are plotted in blue in red. Each row corresponds to a different initial placement of the JP vesicles. (i) Both JP vesicle centroids are on the x -axis. (ii) The centroid of the left JP vesicle is 0.25 nm above the x -axis and the right JP vesicle is on the x -axis. (iii) The centroid of the left JP vesicle is 0.25 nm above the x -axis and the right JP vesicle is 0.25 nm below the x -axis. (iv) The centroid of the left JP vesicle is 1.25 nm above the x -axis and the centroid of the right JP vesicle is 1.25 nm below the x -axis. The streamlines appear in grey and the flow rate is $\dot{\gamma} = 0.005 \text{ ns}^{-1}$ in all cases.

of adhering vesicles in a shear flow (Quaife *et al.* (2019); Abbasi *et al.* (2021)). This adhesive behaviour is absent when two JP vesicles are well-separated.

4.4.2. Extensional Flow

Using a similar setup to the shear flow case, we suspend the same two, pre-relaxed, 58-body JP vesicles and consider their dynamics in an extensional flow

$$\mathbf{u}_{\infty}(\mathbf{x}) = \dot{\gamma}((\mathbf{e}_x \cdot \mathbf{x})\mathbf{e}_x - (\mathbf{e}_y \cdot \mathbf{x})\mathbf{e}_y) \quad (4.10)$$

with extensional rate $\dot{\gamma} = 0.005 \text{ ns}^{-1}$. This extensional flow is stretching in the y -direction and squeezing in the x -direction. Figure 10 shows how the initial placement of the JP vesicles affects the dynamics. When two centroids are both placed symmetrically on the x -axis (case (i)), the JP vesicles come into contact and reach a steady equilibrium. If one centroid is placed

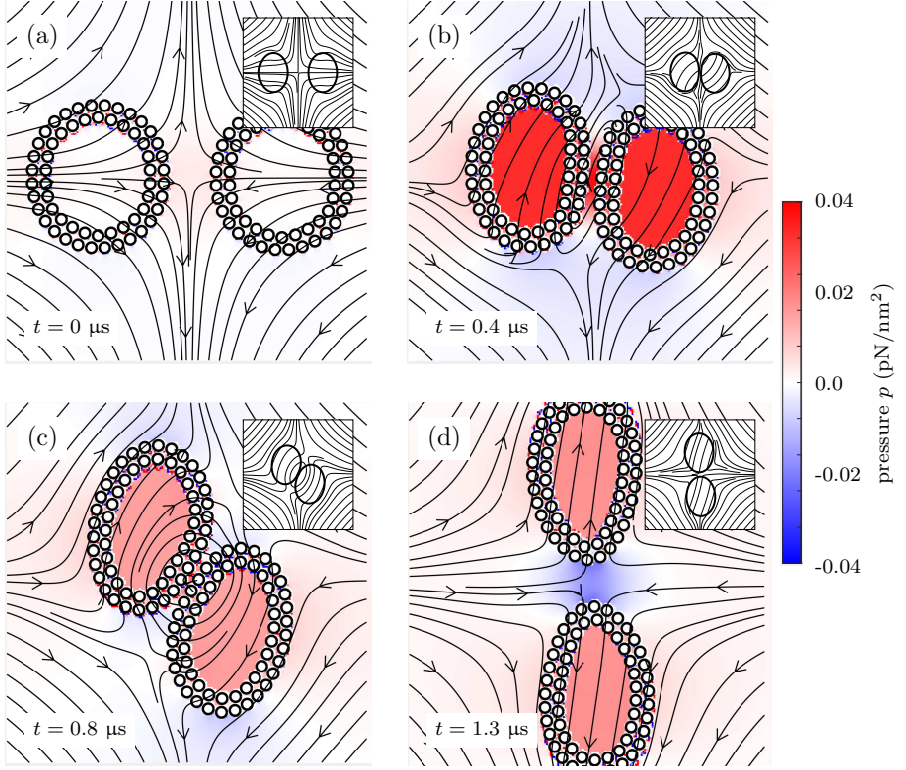


Figure 11: The figure is for the simulation case (iii) of Figure 10, and additionally plots the pressure p . The color bar is shared by all panels. The insets of all panels are generated from simulations of a continuum model of the vesicles and the streamlines agree between the two models.

above the x -axis (case (ii)), the two JP vesicle move together and then upward. The migration of the right JP vesicle is a consequence of the adhesive effect caused by the hydrophobic interactions. When the two centroids start on opposite sides of the x -axis (case (iii)), they eventually diverge from one another along the $\pm y$ -directions. Finally, when the two centroids start on opposite sides of the x -axis, but with a greater displacement (case (iv)), the JP vesicles move much faster along the $\pm y$ -directions.

Figure 11 shows numerical results when the centroids of the two Janus particles are placed at $(-10, -0.1)$ nm and $(10, 0.1)$ nm (case (iii) from Figure 10). With this setup, the two JP vesicles eventually separate along the $\pm y$ -directions and we compare the results against a continuum model as shown in all insets. Panels (b)–(d) show the transient behaviour of the JP vesicles and the continuum vesicles under an extensional flow. In both the coarse-grained model and the continuum model, the vesicles initially converge towards one other and then diverge along the y -axis. The behaviour of the streamlines in both cases are similar. The pressure is initially largest in the gap formed by two JP vesicles and decreases during the separation. The short-range repulsion plays an important role to avoid particle collisions.

5. Conclusion

Fu *et al.* (2020) developed a mathematical model to quantify the macroscopic assembly and mechanics of a JP vesicle in a viscous solvent. The interactions between JP are formulated as a second-kind integral equation, which is coupled to the Stokes equations for the surrounding incompressible fluid at the zero-Reynolds-number limit. Numerical simulations of a JP suspensions revealed self-assembly of JP into micelles and bilayers, providing an alternative means for computing mechanical moduli, which often requires the knowledge of an equation of state from experiments on a colloidal membrane (Balchunas *et al.* (2019)). Results in this work show great potential to study Janus colloids (Bradley *et al.* (2017); Mallory *et al.* (2017)) and the morphology of colloid surfactants (Bradley *et al.* (2016)). For example, with the flexibility of the model, we can specify the boundary condition on JP surfaces based on the chemicals used in experiments.

In the present study, we used this integral formulation and numerical algorithm to simulate the hydrodynamics of JP vesicles in background flows. Under a linear shear flow, we found a JP vesicle to exhibit elongation and tank-treading dynamics observed for a lipid bilayer GUV. The results showed that the reduced area A^* decreases with shear rate but that the total length of a JP vesicle is conserved. The decay rate of the reduced area was independent of the shear rate values between 0.003 ns^{-1} and 0.005 ns^{-1} . Moreover, the proposed model describes membrane rupture in high shear rates. Therefore, our method can be applied to vesicles undergoing topological changes which is difficult to simulate when using a continuum model that represents vesicles as closed and continuous curves.

We estimated the inter-monolayer friction b , membrane permeability constant P , and the membrane stretching modulus K_A . The inter-monolayer friction coefficient was determined by calculating the tangential shear force and slip velocities with respect to the bilayer mid-plane. The range of friction coefficients agree with values reported by den Otter & Shkulipa (2007) in their MD study. The coarse-graining level of the JP vesicle has a larger length scale than molecular dynamics simulations, and in the future convergence studies we will investigate how physical properties like the friction coefficient and membrane permeability depend on the particle shape and size.

We also simulate the spatial migration of a JP vesicle in a parabolic shear flow. Replicating the hydrodynamics of a GUV in a Poiseuille flow (Kaoui *et al.* (2009); Danker *et al.* (2009); Coupier *et al.* (2008)), the JP vesicle moves toward the centre of the shear flow. While the initial reduced area of the JP vesicle is $A^* \approx 1$, the equilibrium reduced area is $A^* = 0.9$. For the parameters we used in the simulation, the JP vesicle takes on an asymmetric, “slipper” shape as it settles above the centre of flow and exhibits tank-treading motion. An interesting result contrast with continuum results is that the JP vesicle oscillates at a height slightly above the centre of the Poiseuille flow.

We further simulated the hydrodynamics of two JP vesicles, and drew comparisons with simulation results of two vesicles described by the Helfrich continuum model. A comparison of the vesicle shapes and the streamlines demonstrate remarkable similarities. The two overlapping trajectories of the JP vesicles’ centroids in a shear flow evolve as expected when the two centroids are initialized on the same horizontal level. We also observe a rotating behaviour that is observed for models involving vesicle adhesion (Quaife *et al.* (2019)). The hydrophobic attraction led to this adhesive effect when two JP bilayers are sufficiently close. We also performed several simulations of a pair of JP vesicles suspended in an extensional flow. By varying the initial vertical displacement of the vesicles’ centroids, we can control for divergent trajectories and obtain similar results to the continuum model.

In § 3.3, we derived an alternative integral form for calculating the force and torque to avoid the singular integral evaluation. These alternative integrals allow us to accurately

resolve trajectories over long times without having to rely on computationally expensive quadratures.

Our future goals include extending the current framework to a three-dimensional JP vesicle system. This will require additional algorithmic implementation including a fast summation method such as the fast multipole method. Another research direction is to include the fluctuating hydrodynamics for Brownian suspensions (Bao *et al.* (2018)), and this is critical to understand membrane diffusion. Finally, a more physical boundary conditions for the HAP model will allow us to draw comparisons between computational and laboratory experiments.

Acknowledgments: B.Q. acknowledges support from NSF (Grant No. DMS 2012560) and from the Simons Foundation, Mathematics and Physical Sciences-Collaboration Grants for Mathematicians (Award No. 527139). Y.-N. Y. acknowledges support from NSF (Grant No. DMS 1614863 and 1951600) and Flatiron Institute, part of Simons Foundation.

REFERENCES

- ABBASI, MEHDI, FARUTIN, ALEXANDER, EZ-ZAHRAOUI, HAMID, BENYOUSSEF, ABDELILAH & MISBAH, CHAOQUI 2021 Erythrocyte-erythrocyte aggregation dynamics under shear flow. *Physical Review Fluids* **6**, 023602.
- BALCHUNAS, J., CABANAS, R. A., ZAKHARY, M. J., GIBAUD, T., FRADEN, S., SHARMA, P., HAGAN, M. F. & DOGIC, Z. 2019 Equation of state of colloidal membranes. *Soft Matter* **15**, 6791.
- BAO, YUANXUN, RACHH, MANAS, KEAVENY, ERIC E., GREENGARD, LESLIE & DONEV, ALEKSANDAR 2018 A fluctuating boundary integral method for brownian suspensions. *Journal of Computational Physics* **374**, 1094–1119.
- BRADLEY, LAURA C., CHEN, WEI-HAN, STEBE, KATHLEEN J. & LEE, DAEYEON 2017 Janus and patchy colloids at fluid interfaces. *Current Opinion in Colloid & Interface Science* **30**, 25–33.
- BRADLEY, LAURA C., STEBE, KATHLEEN J. & LEE, DAEYEON 2016 Clickable janus particles. *Journal of the American Chemical Society* **138** (36), 11437–11440.
- BRANDNER, ASTRID F., TIMR, STEPAN, MELCHIONNA, SIMONE, DERREUMAUX, PHILIPPE, BAADEN, MARC & STERPONE, FABIO 2019 Modelling lipid systems in fluid with Lattice Boltzmann Molecular Dynamics simulations and hydrodynamics. *Scientific Reports* **9** (1), 16450.
- BYSTRICKY, LUKAS, SHANBHAG, SACHIN & QUAIPE, BRYAN 2020 Stable and contact-free time stepping for dense rigid particle suspensions. *International Journal for Numerical Methods in Fluids* **92** (2), 94–113.
- CHABANON, MORGAN, HO, JAMES C. S., LIEBERG, BO, PARIKH, ATUL N. & RANGAMANI, PADMINI 2017 Pulsatile Lipid Vesicles under Osmotic Stress. *Biophysical Journal* **112**, 1682–1691.
- CORONA, EDUARDO, GREENGARD, LESLIE, RACHH, MANAS & VEERAPANENI, SHRAVAN 2017 An integral equation formulation for rigid bodies in Stokes flow in three dimensions. *Journal of Computational Physics* **332**, 504–519.
- CORONA, EDUARDO & VEERAPANENI, SHRAVAN 2018 Boundary integral equation analysis for suspension of spheres in Stokes flow. *Journal of Computational Physics* **362**, 327–345.
- COUPIER, GWENNOU, KAOUI, BADR, POKGORSKI, THOMAS & MISBAH, CHAOQUI 2008 Noninertial lateral migration of vesicles in bounded poiseuille flow. *Physics of Fluids* **20**, 111702.
- DANKER, GERRIT, VLAHOVSKA, PETIA M. & MISBAH, CHAOQUI 2009 Vesicles in Poiseuille Flow. *Physical Review Letters* **102**, 148102.
- FENG, ZHI-GANG & MICHAELIDES, EFSTATHIOS E. 2004 The immersed boundary-lattice Boltzmann method for solving fluid–particles interaction problems. *Journal of Computational Physics* **195**, 602–628.
- FINKEN, R., LAMURA, A., SEIFERT, U. & GOMPPER, G. 2008 Two-dimensional fluctuating vesicles in linear shear flow. *The European Physical Journal E* **25** (3), 309–321.
- FU, SZU-PEI P., RYHAM, ROLF, KLÖCKNER, ANDREAS, WALA, MATT, JIANG, SHIDONG & YOUNG, YUAN-NAN 2020 Simulation of Multiscale Hydrophobic Lipid Dynamics via Efficient Integral Equation Methods. *Multiscale Modeling & Simulation* **18** (1), 79–103.
- DE GENNES, P.-G. 1991 Soft matter. *Nobel Lecture*.
- GLOWINSKI, R., PAN, T. W., HESLA, T. I., JOSEPH, D. D. & PÉRIAUX, J. 2001 A Fictitious Domain Approach

- to the Direct Numerical Simulation of Incompressible Viscous Flow past Moving Rigid Bodies: Application to Particulate Flow. *Journal of Computational Physics* **169**, 363–426.
- JEFFERY, G. B. 1922 The motion of ellipsoidal particles immersed in a viscous fluid. *Proceedings of the Royal Society A* **102** (715), 161–179.
- KABACAOĞLU, GOKBERK, QUAIFE, BRYAN & BIROS, GEORGE 2018 Low-resolution simulations of vesicle suspensions in 2D. *Journal of Computational Physics* **357**, 43–77.
- KAOU, BADR, BIROS, GEORGE & MISBAH, CHAOUI 2009 Why Do Red Blood Cells Have Asymmetric Shapes Even in a Symmetric Flow? *Phys. Rev. Lett.* **103**, 188101.
- KLÖCKNER, ANDREAS, BARNETT, ALEXANDER, GREENGARD, LESLIE & O’NEIL, MICHAEL 2013 Quadrature by expansion: A new method for the evaluation of layer potentials. *Journal of Computational Physics* **252**, 332–349.
- LU, LIBIN, RAHIMIAN, ABTIN & ZORIN, DENIS 2017 Contact-aware simulations of particulate Stokesian suspensions. *Journal of Computational Physics* **347**, 160–182.
- MALLORY, S A, ALARCON, F, CACCIUTO, A & VALERIANI, C 2017 Self-assembly of active amphiphilic janus particles. *New Journal of Physics* **19** (12), 125014.
- NAGLE, JOHN F. & TRISTRAM-NAGLE, STEPHANIE 2000 Structure of lipid bilayers. *Biochimica et Biophysica Acta (BBA) - Reviews on Biomembranes* **1469** (3), 159–195.
- DEN OTTER, W. K. & SHKULIPA, S. A. 2007 Intermonolayer Friction and Surface Shear Viscosity of Lipid Bilayer Membranes. *Biophysical Journal* **93** (2), 423–433.
- POWER, H. & MIRANDA, G. 1987 Second kind integral equation formulation of stokes’ flows past a particle of arbitrary shape. *SIAM Journal on Applied Mathematics* **47** (4), 689–698.
- QUAIFE, BRYAN & BIROS, GEORGE 2014 High-volume fraction simulations of two-dimensional vesicle suspensions. *Journal of Computational Physics* **274**, 245–267.
- QUAIFE, BRYAN, GANNON, ASHLEY & YOUNG, Y.-N. 2021 Hydrodynamics of a Semipermeable Vesicle Under Flow and Confinement. *Physical Review Fluids* **6**, 073601.
- QUAIFE, BRYAN, VEERAPANENI, SHRAVAN & YOUNG, Y.-N. 2019 Hydrodynamics and rheology of a vesicle doublet suspension. *Physical Review Fluids* **4**, 103601.
- RACHH, MANAS & GREENGARD, L. 2016 Integral equation methods for elastance and mobility problems in two dimensions. *SIAM Journal on Numerical Analysis* **54** (5), 2889–2909.
- SCHWALBE, JONATHAN T., VLAHOVSKA, PETIA M. & MIKSI, MICHAEL J. 2010 Monolayer slip effects on the dynamics of a lipid bilayer vesicle in a viscous flow. *Journal of Fluid Mechanics* **647**, 403–419.
- WOHLERT, JAKOB & EDHOLM, OLLE 2006 Dynamics in atomistic simulations of phospholipid membranes: Nuclear magnetic resonance relaxation rates and lateral diffusion. *The Journal of Chemical Physics* **125** (20), 204703.
- YAN, WEN, CORONA, EDUARDO, MALHOTRA, DHAIRYA, VEERAPANENI, SHRAVAN & SHELLEY, MICHAEL 2020 A scalable computational platform for particulate Stokes suspensions. *Journal of Computational Physics* **416**, 109524.
- ZGORSKI, ANDREW, PASTOR, RICHARD W. & LYMAN, EDWARD 2019 Surface shear viscosity and interleaflet friction from nonequilibrium simulations of lipid bilayers. *Journal of Chemical Theory and Computation* **15** (11), 6471–6481.
- ZHAO, HONG & SHAQFEH, ERIC S. G. 2011 The dynamics of a vesicle in simple shear flow. *Journal of Fluid Mechanics* **674**, 578–604.